scientific reports

Check for updates

OPEN

Tunable growth of one-dimensional graphitic materials: graphene nanoribbons, carbon nanotubes, and nanoribbon/nanotube junctions

Shuo Lou[1,2,8], Bosai Lyu[1,2,8], Jiajun Chen[1,2,8], Lu Qiu[3,4,8], Saiqun Ma[1,2], Peiyue Shen[1,2], Zhichun Zhang[1,2], Yufeng Xie[1,2], Qi Liang[1,2], Kenji Watanabe[5], Takashi Taniguchi[6], Feng Ding[3,4]✉ & Zhiwen Shi[1,2,7]✉

Graphene nanoribbons (GNRs) and carbon nanotubes (CNTs), two representative one-dimensional (1D) graphitic materials, have attracted tremendous research interests due to their promising applications for future high-performance nanoelectronics. Although various methods have been developed for fabrication of GNRs or CNTs, a unified method allowing controllable synthesis of both of them, as well as their heterojunctions, which could largely benefit their nano-electronic applications, is still lacking. Here, we report on a generic growth of 1D carbon using nanoparticles catalyzed chemical vapor deposition (CVD) on atomically flat hexagonal boron nitride (h-BN) substrates. Relative ratio of the yielded GNRs and CNTs is able to be arbitrarily tuned by varying the growth temperature or feeding gas pressures. The tunability of the generic growth is quantitatively explained by a competing nucleation theory: nucleation into either GNRs or CNTs by the catalysts is determined by the free energy of their formation, which is controlled by the growth conditions. Under the guidance of the theory, we further realized growth of GNR/CNT intramolecular junctions through changing H_2 partial pressure during a single growth process. Our study provides not only a universal and controllable method for growing 1D carbon nanostructures, but also a deep understanding of their growth mechanism, which would largely benefit future carbon-based electronics and optoelectronics.

Graphitic materials, i.e., sp^2-hybridized carbon, includes 3D graphite, 2D graphene, 1D carbon nanotubes (CNTs) and graphene nanoribbons (GNRs), as well as 0D buckyballs. They own excellent electronic[1–3], mechanical[4,5] and thermal[6] properties, and therefore hold great promise for a wide range of applications. Of particular interests, 1D CNTs and GNRs, due to their structurally-tunable bandgaps and ultra-high carrier mobility, show promise for future high-performance nanoelectronics[7,8]. Specifically, CNTs being either metallic or semiconducting determined by their chiralities, can serve as building blocks for miniaturized conducting wires and field-effect transistors (FET)[2,9]; GNRs with bandgaps inversely proportional to their width[10] and spin-polarized zigzag-edge states[11–14], are excellent candidate materials for spintronic devices.

Synthesis of those 1D graphitic materials forms the basis of their electronic applications. On the one hand, the synthesis of CNTs is rather mature as many growth methods have been developed since its discovery[15] in

[1]Key Laboratory of Artificial Structures and Quantum Control (Ministry of Education), Shenyang National Laboratory for Materials Science, School of Physics and Astronomy, Shanghai Jiao Tong University, Shanghai 200240, China. [2]Collaborative Innovation Center of Advanced Microstructures, Nanjing University, Nanjing 210093, China. [3]Centre for Multidimensional Carbon Materials, Institute for Basic Science, Ulsan 44919, South Korea. [4]School of Materials Science and Engineering, Ulsan National Institute of Science and Technology, Ulsan 44919, South Korea. [5]Research Center for Functional Materials, National Institute for Materials Science, 1-1 Namiki, Tsukuba 305-0044, Japan. [6]International Center for Materials Nanoarchitectonics, National Institute for Materials Science, 1-1 Namiki, Tsukuba 305-0044, Japan. [7]Tsung-Dao Lee Institute, Shanghai Jiao Tong University, Shanghai 200240, China. [8]These authors contributed equally: Shuo Lou, Bosai Lyu, Jiajun Chen and Lu Qiu. ✉email: f.ding@unist.ac.kr; zwshi@sjtu.edu.cn

1991, such as catalytic chemical vapor deposition (CVD)[16], laser ablation method[17], and arc discharge method[18]. The most successful and widely used CNT growth method is the transition-metal-nanoparticle-catalyzed CVD, with which high-quality CNTs of uniform diameter and meters-long length have been achieved[16,19–22]. On the other hand, synthesis of micrometer-long, narrow, and smooth-edged GNRs turns to be rather difficult, although great efforts have been devoted[14,23–30]. A recent study shows that the nanoparticle-catalytic CVD can also be used to grow GNRs of high purity and high quality[31]. This establishes an important connection between the growth of CNTs and the growth of GNRs, and opens up opportunities to develop a generic method for growing both GNRs and CNTs with tunable yield, which is critical for future carbon-based electronic devices and circuits.

Here, we report a unified and controllable growth of GNRs and CNTs on h-BN substrate using nanoparticle-catalyzed CVD method, in which the ratio of GNRs/CNTs can be arbitrarily tuned. Experimentally, we observed a tunable and competing growth phenomenon between GNRs and CNTs: pure GNRs, pure CNTs, and mixed GNRs/CNTs can be selectively obtained through changing the growth temperature or hydrogen partial pressures. Theoretically, through calculating the free energy of formation of CNTs and GNRs, we reveal a competition between GNRs and CNTs during the nucleation stage: lower temperatures and higher hydrogen pressures energetically favor the growth of GNRs, whereas higher temperatures and lower hydrogen pressures support the growth of CNTs. The theory agrees well with the experimental results. Furthermore, under the guidance of the competing nucleation theory, we realized switching of GNR growth into CNT growth for an individual catalytic-nanoparticle. As a result, GNR/CNT intermolecular junctions are successfully fabricated through changing H_2 pressures during a single growth progress.

Results

Growth and identification of GNRs and CNTs. Figure 1a schematically illustrates the catalytic growth of GNRs and CNTs on an h-BN substrate. In prior to the growth, Fe nanoparticles are deposited onto h-BN substrates as catalysts. A typical growth process is depicted in Fig. 1h. Firstly, samples are heated to the growth temperature (~ 800 °C) in a CVD furnace with a flow of mixed Ar and H_2. Then, CH_4 gas is fed in as carbon source for the growth of CNTs or GNRs. A typical growth duration is 30 min. Lastly, the samples are cooled down to room temperature with protective gas of Ar and H_2. The pressure during the whole process is atmospheric pressure (P_0). (See methods for more growth details. Supplementary Information (Fig. S4) gives a schematic of the growth process of a CNT and a GNR).

Figure 1b shows an atomic force microscopy (AFM) topography image of the as-grown samples. Straight micrometer-long 1D structures grew out from catalytic Fe nanoparticles arranged along a h-BN step edge. We initially distinguish CNTs and GNRs through their heights (Fig. 1e) as flat GNRs (0.2–0.3 nm) are normally lower than tubular CNTs (~ 1 nm). Noted that the CNTs are single-walled. Another notable difference between tubes and ribbons is the shape of their turns. In general, GNRs (Fig. 1d) tend to produce sharper corners while CNTs tend to produce gentle-curved bends (Fig. 1c), as tubular CNTs have much larger bending stiffness than GNRs[25]. We can further identify the CNTs and GNRs using a scanning near-field optical microscopy (SNOM), where CNTs are much brighter than GNRs (Fig. 1g) due to CNTs' larger optical conductivity than GNRs[32]. Figure 1f is the AFM topography image corresponding to the near-field infrared image. So far, we have successfully synthesized both GNRs and CNTs on h-BN substrates through a generic nanoparticle-catalyzed CVD method, and identified CNTs and GNRs through the differences in their height, shape and infrared response.

Tunable population ratio between CNTs and GNRs. It is rather surprising that the nanoparticle-catalyzed CVD growth can produce both planar GNRs and cylindrical CNTs simultaneously. To explore the tunability of the growth products, we carried out a series of growths with systematically varied temperatures and H_2 pressures. The ratio of yielded CNT is plotted in Fig. 2a as 3D column diagram. From the diagram, we can see that high ratio of CNT appears at low H_2 pressures and high growth temperature, whereas low ratio of CNT appears at high H_2 pressures and low temperature. This implies that low H_2 pressures and high temperature favor the growth of CNTs, and high H_2 pressures and low temperature favor the growth of GNRs. To be more intuitive, we display in Fig. 2b–j AFM images of growth products at a few representative conditions. At low H_2 pressures ($P_{H2} = 0$), the samples are nearly pure CNTs (Fig. 2b,e,h). With H_2 pressures increasing to 0.33 P_0, there are mixtures of GNRs and CNTs (Fig. 2c,f,i). When H_2 pressures are high enough, only GNRs are obtained (Fig. 2d,g,j). At a moderate H_2 pressures of 0.33 P_0, one can clearly see more CNTs in high temperature samples, such as T = 850 °C (Fig. 2c), than low temperature samples (Fig. 2i). Thus, we demonstrate the large tunability of the growth products (pure GNRs, pure CNTs and mixtures samples) through modulating growth temperature and H_2 pressures: lower H_2 pressures and higher temperature tend to produce CNTs, and higher H_2 pressure and lower temperature tend to produce GNRs.

Competing nucleation theory of the catalytic-CVD growth. In the growth, formation of either planar GNRs or tubular CNTs is largely determined in the nucleation stage. Therefore, an investigation of the microscopic process of the nucleation is required. During nucleation of either GNRs or CNTs, graphitic nano-islands will firstly form on the surface of catalyst nanoparticles. To create a CNT, the graphitic island will have to lift off from the particle to form a graphitic cap (or CNT nucleus) by introducing an extra curvature energy into the system[33,34]. Besides, the tubular structure of CNTs further leads to the reduction of their contact area with substrate (only the bottom part of CNTs as shown in Fig. 3a), and therefore loss of part of the van der Waals adhesion. As elaborated recently[34], the driving force of tube formation is the reduction of the contact energy between the cap edge and the catalyst surface, which requires a strong interaction between the dangling atoms of the cap edge and the catalyst surface or the edge atoms of the cap cannot be passivated by any functional groups (such as –H, –OH or –O). Here, the presence of h-BN substrate opens up another channel to convert the gaseous

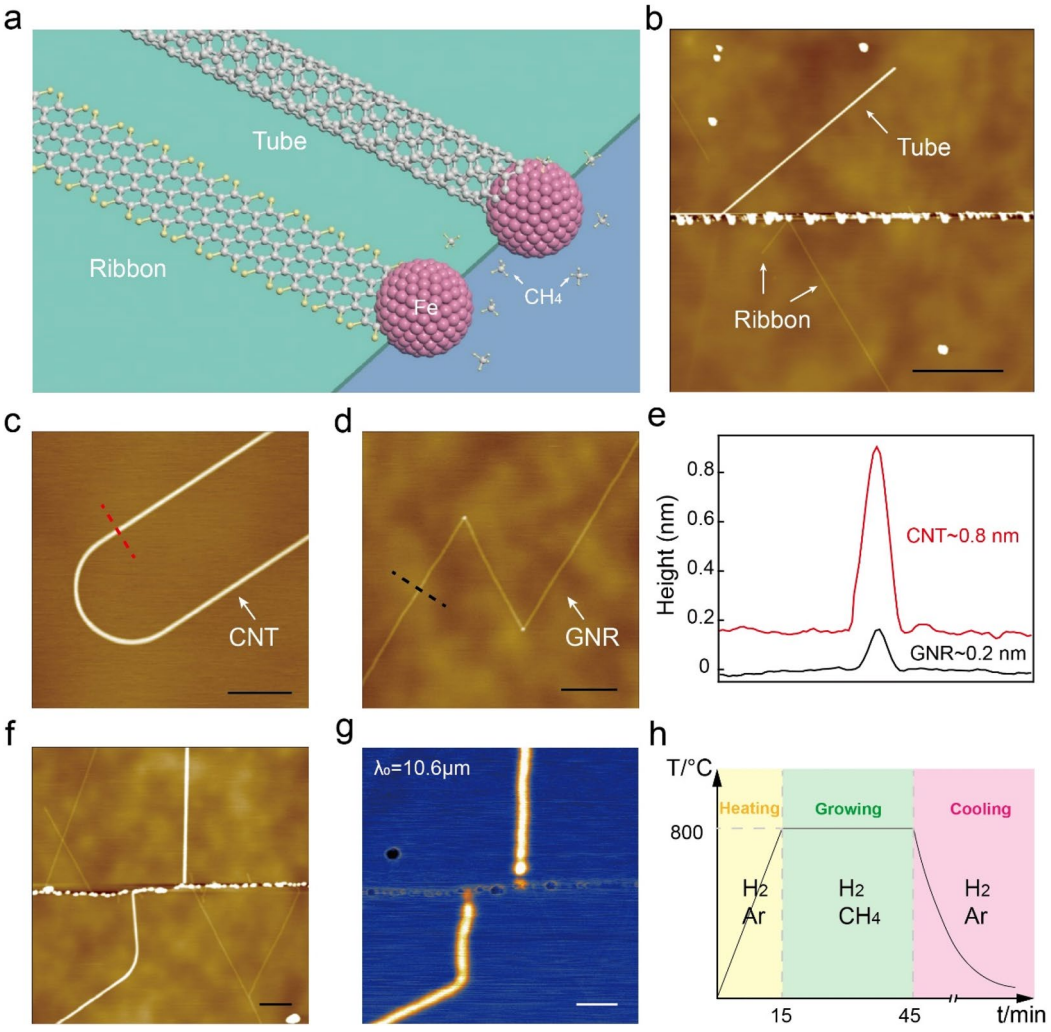

Figure 1. Growth and characterizations of GNRs and CNTs. (**a**) Schematic of GNR and CNT growth on h-BN substrate. The growth starts at Fe-nanoparticles, where methane molecules can decompose into atomic carbon, serving as source for the GNRs and CNTs growth. (**b**) AFM topography image of an as-grown sample with both GNRs and CNTs on h-BN. The higher (brighter) line corresponds to CNTs, and the lower (blurred) ones correspond to GNRs. Bright dots are Fe-nanoparticles. (**c**,**d**) AFM topography images of turns in CNTs and GNRs. A CNT tends to produce gentle-curved bends (**c**), while a GNR tends to produce sharp corners (**d**). This is due to the difference in their stiffness. (**e**) Height profiles of a CNT (red) and a GNR (black), taken along the dash lines in panel (**c**) and (**d**). The diameter of a nanotube is apparently larger than the thickness of a nanoribbon. (**f**,**g**) AFM topography image of CNTs and GNRs and the corresponding near-field infrared image of the same area. CNTs exhibit stronger response (brighter) than GNRs in the near-field optical image due to CNTs' stronger optical conductivity. (**h**) Illustration of a typical growth process. Scale bars: 500 nm in (**b**); 100 nm in (**c**,**d**,**f**,**g**).

carbon (CH_4) into planar GNRs, which have a larger contact area with the h-BN substrate and thus a significant gain in adhesion energy compared to that in CNTs (Fig. 3a). Supplementary Information (Fig. S3) shows growth results on different substrates. But a pristine GNR has dangling bonds on both edges, whose formation energies are in the order of ~ 10 eV/nm[35]. These highly unstable edges must be passivated by tuning the precursor gases, and therefore the formation energies of the two edges of GNRs will depends on the H_2 pressure under our CVD condition. In general, CNT formation would be favorable if the partial pressure of H_2 gas is small and GNRs might be formed with large H_2 pressure.

Theoretically, nucleation of either CNTs or GNRs depends largely on their free energy of formation. In the following, through comparison of their formation energies, a theoretical growth diagram of GNR vs. CNT was achieved and a competing nucleation mechanism was revealed. We first calculated the free energies of formation of both GNRs and CNTs at different temperatures and under different pressures of H_2, by including the adhesion energy with substrate, curvature energy and H-passivated edge energy (Fig. 3b). In the experiments, the average width (W) of the synthesized AC-GNR is ~ 2.2 nm, the average diameter (d) of the CNT is ~ 1.2 nm, and therefore, the width to diameter ratio is ~ 1.88. We did the DFT calculations of GNRs and CNTs with such effective

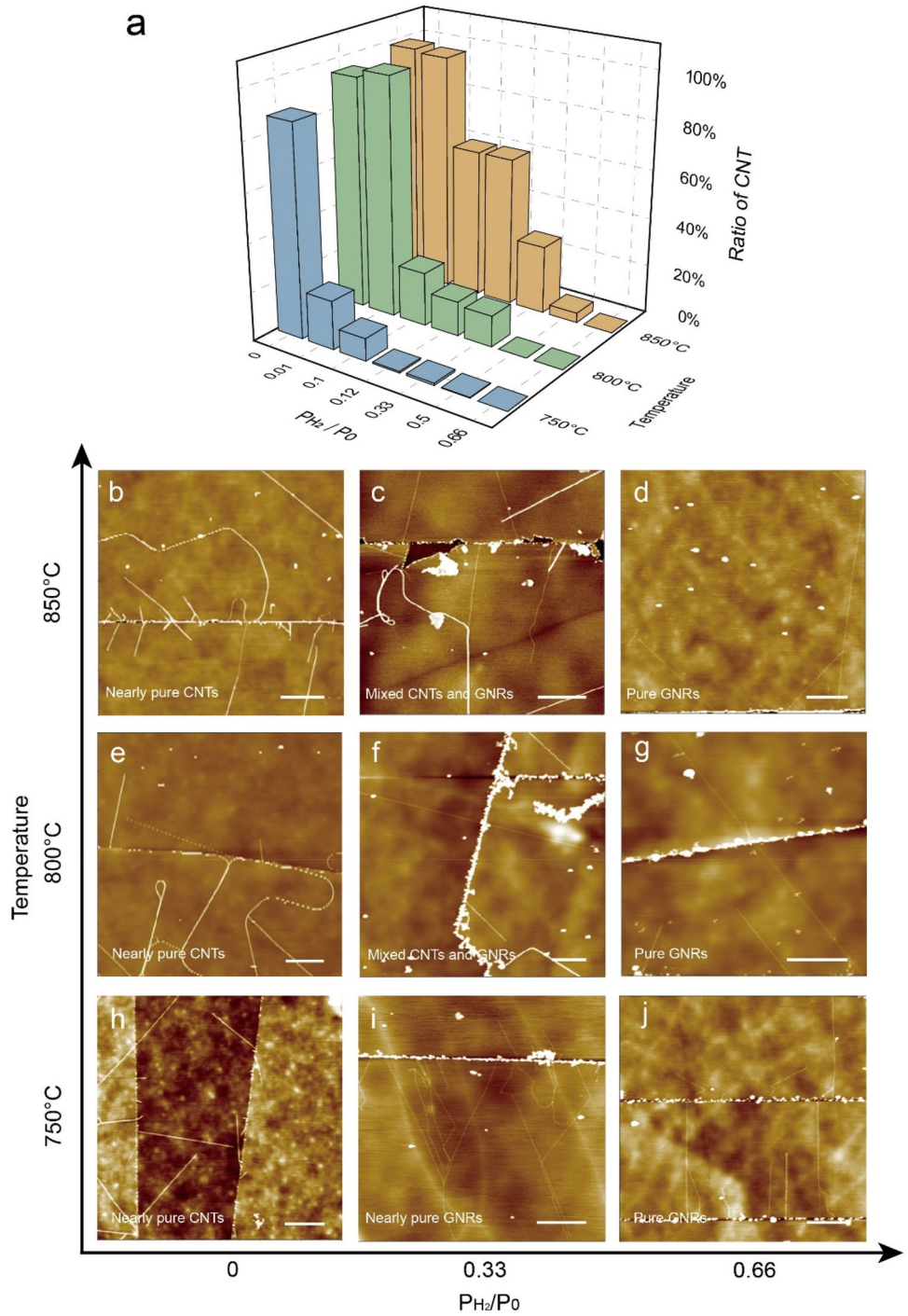

Figure 2. Variable ratio of GNRs and CNTs under different growth conditions. (**a**) Statistics of the proportion of CNTs as a function of growth temperatures and H_2 pressures. (**b**–**j**) AFM images of representative samples grown under different conditions. High temperatures (850 °C) and low H_2 pressures ($P_{H2}/P_0 = 0$) support the CNTs growth. Low temperature (750 °C) and high H_2 pressures ($P_{H2}/P_0 = 0.66$) favor the GNRs growth. Scale bars: 500 nm.

ratio W = 1.88 d. The free energy of CNTs remains a constant, whereas that of GNRs changes systematically with growth temperature T and hydrogen pressure P_{H2}, due to the corresponding change of edge formation energy in GNRs. Note that at certain condition where the energy lines of GNRs and CNTs cross, the two species have the same free energy of formation. This provides possibilities to realize switching between formations of GNRs and CNTs in the growth. Based on the calculation of the free energy of formation, we draw a nucleation phase diagram of GNRs vs. CNTs (Fig. 3c,d). From the phase diagram, one can see that the nucleation of either GNRs (blue region) or CNTs (red region) is determined by the temperature and H_2 pressures in the reactor and the

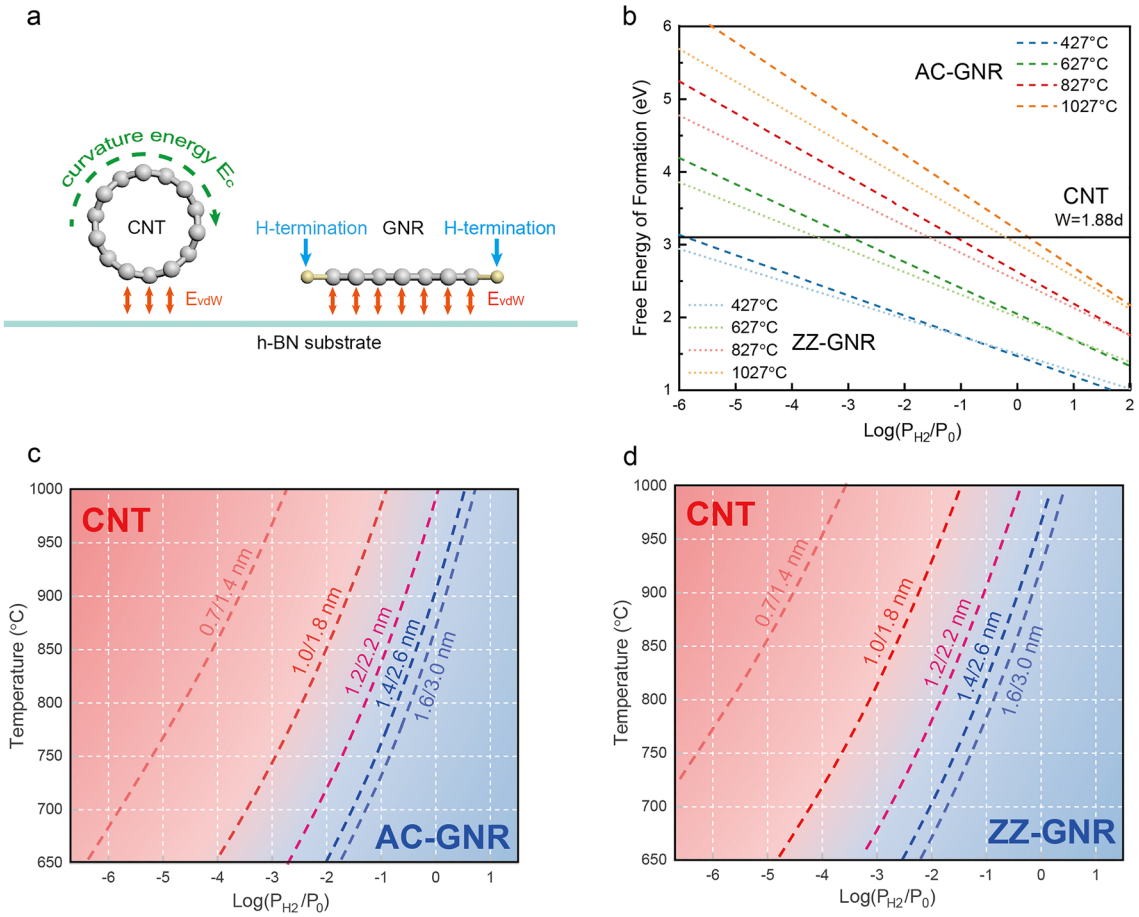

Figure 3. Competing nucleation between GNRs and CNTs. (**a**) Schematic of a tubular CNT and a planer GNR on h-BN substrate. (**b**) Free energy of formation of CNTs (black line) and zigzag/armchair (dot lines/dash lines) GNRs as a function of H_2 pressures at a few representative temperatures. (**c**,**d**) Theoretical growth phase diagram. Red and blue regions stand for energetically favorable for growing CNTs and GNRs, respectively. The dashed lines represent equal probability of yielding GNRs and CNTs of different width and diameter. The diameter and the width of the compared CNTs and GNRs are denoted along the dash lines (CNTs' diameter/GNRs' width).

width/diameter of the GNR/CNT. The lower temperature and the higher partial pressures of H_2, the more stable the GNRs. Meanwhile, in the condition of higher temperature and lower H_2 partial pressures, the nucleation of CNTs is more energetically favorable (more calculation details see methods). The theoretical phase diagram of competing nucleation agrees well with the experimental growth results.

GNR/CNT intramolecular junctions. Under the inspiration of the competing nucleation theory, we successfully grow a novel GNR/CNT heterojunction structure. Based on the theory, varying H_2 pressures or temperature can tune the growth from GNR favorable to CNT favorable. Thus, heterojunction structures consisting of GNR section and CNT section can in principle be synthesized through adjusting growth conditions during a single growth process. Here, by abruptly changing the H_2 pressures in a single growth process, we successfully synthesized GNR/CNT heterojunctions. Figure 4a schematically shows the steps for growing a GNR/CNT junction. First, mixed gases of CH_4 (120 sccm) and H_2 (80 sccm) were injected to grow the GNR section in the first stage. Then, all remaining gases in the CVD furnace were rapidly pumped out. After that, only CH_4 gas was supplied to grow CNT section in the second stage. Figure 4b displays an AFM image of an as-grown CNT/GNR junction sample, and Fig. 4c is a zoom-in image of the area denoted by the square box in Fig. 4b. It clearly shows two distinct sections with different heights: one with height of ~0.7 nm and the other one with height of ~0.2 nm, revealing that this sample consists of both CNT and GNR sections. More GNR/CNT junctions structures can be found in Supplementary Information (Fig. S1). The success in fabrication of GNR/CNT junctions further demonstrates the controllability of our nano-particle catalyzed CVD growth method and also verifies the competing nucleation theory. In addition, the obtained GNR/CNT heterojunction can serve as building blocks for future carbon-based electronic and optoelectronic devices, such as field-effect transistors, logic gates and high-performance photodetectors[36]. We would like to note that the transition from GNR to CNT allows the CNT growth without a cap formation. Typically, the chirality of the CNT depend on the atomic structure of its cap, which generally leads to a random distribution of chiralities[37]. Our previous study clearly showed that the

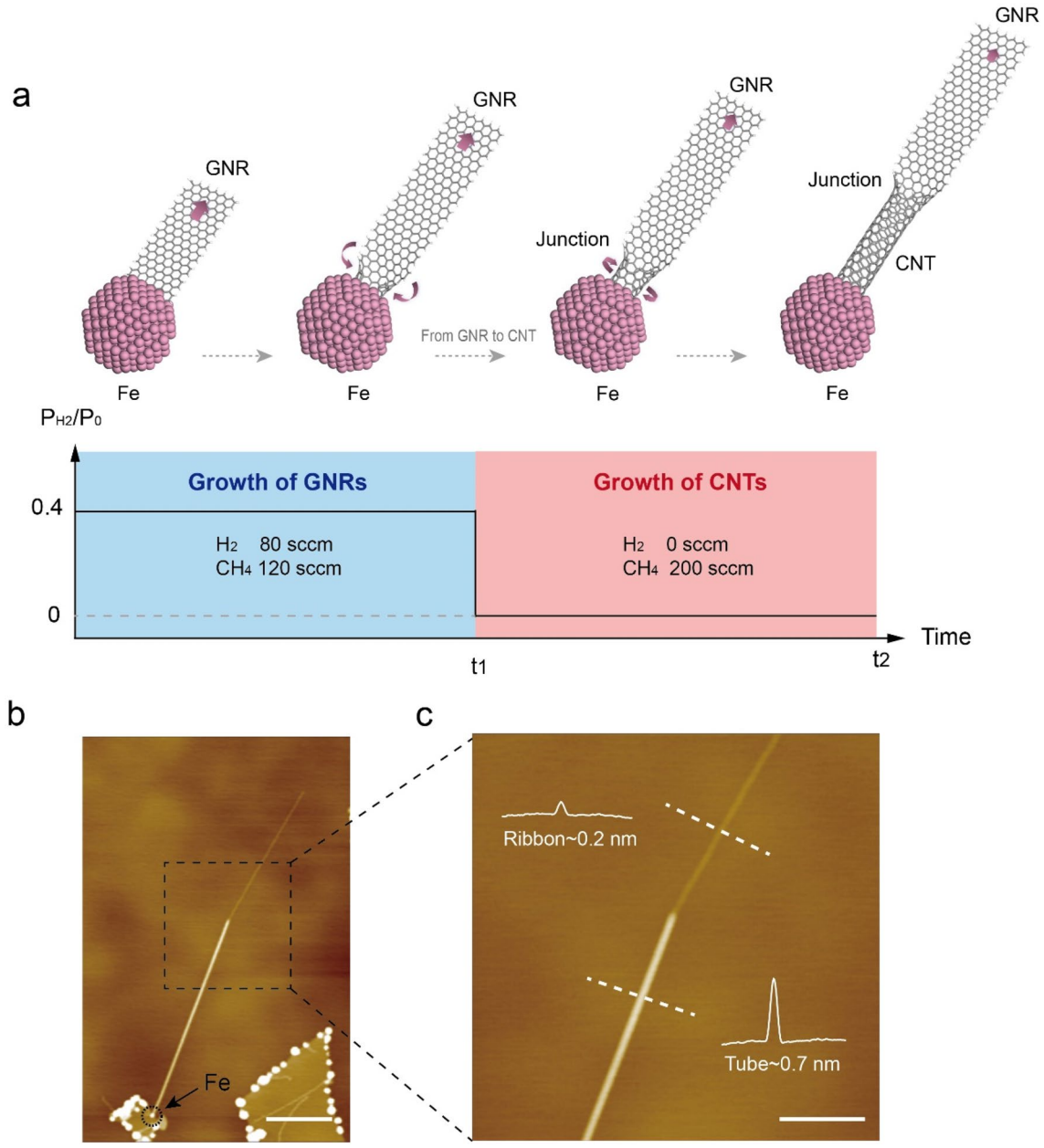

Figure 4. Growth of GNR/CNT junctions. (**a**) Schematic of growth of GNR/CNT junctions through abrupt change of H_2 pressure. The product switches from ribbon to tube, which yields a junction structure in the middle. (**b**) Topography of a typical GNR/CNT junction structure. (**c**) A zoom-in AFM image of the joint region in the dashed box in panel (**b**). Height profiles taken along the dashed lines show the tube height ~ 0.7 nm and ribbon height ~ 0.2 nm. Scale bars: 200 nm in (**b**); 100 nm in (**c**).

controllable synthesis of GNR is possible, thus this study provides a feasible way to grow chirality controlled CNTs.

Discussion

We report the growth of 1D graphitic nanomaterials on h-BN substrates using a unified catalytic-CVD method, with which pure CNTs, pure GNRs, mixed CNTs/GNRs, and CNT/GNR heterojunctions are successfully achieved. Experimentally, we found that the population ratio of CNT or GNR can be efficiently tuned through modulating growth temperature or H_2 pressure. Theoretically, we calculated the free energy of formation, and revealed a competition between GNRs and CNTs during the nucleation stage, which agrees well with our experimental results. Under the guidance of the competing nucleation theory, a novel GNR/CNT junction structure was successfully synthesized through abrupt change of H_2 pressures within a single growth process. The reported tunable growth of GNRs and CNTs through a simple catalytic-CVD method provide not only a deep understanding

of the growth mechanism of 1D graphitic materials, but more importantly an exciting approach for synthesizing building blocks for future carbon-based nanoelectronics.

Methods

CVD growth of GNRs, CNTs and GNR/CNT intramolecular junctions. Hexagonal-BN flakes were mechanically exfoliated onto SiO_2/Si as growth substrates. Next, h-BN on SiO_2/Si substrates were annealed at 300 °C with hydrogen to remove organic contaminations. Then, 0.5–1 Å thick Fe film, as catalyst, was deposited onto the substrates using thermal evaporation at a rate of ~0.05 Å/s. The substrates were loaded into a furnace tube (Anhui BEQ Equipment Technology), followed by pumping out the remaining air in the tube. Then, the substrates were gradually heated up to the growth temperature (typically, 750/800/850 °C) for 15 min under an Ar/H_2 flow (200 sccm). After reaching the target growth temperature, a CH_4/H_2 flow (200 sccm) was injected into the chamber for the growth of GNRs and CNTs, and the growth temperature was kept for 30 min. The ratio of hydrogen was tuned to obtain different ratios of yielded GNRs and CNTs. For GNR/CNT intramolecular junctions growth, a single growth process was consist of two stages. In the first stage, a CH_4/H_2 flow with high partial pressure of hydrogen was injected to grow the GNR section. In the second stage, pure CH_4 gas was supplied to grow the CNT section. Before starting the second stage, all remaining gases in the CVD furnace of the first stage were rapidly pumped out. Finally, the systems were cooled down to room temperature under a protective hydrogen and argon atmosphere (Supplementary Information).

Atomic force microscopy (AFM). A commercial AFM (Cypher S, Asylum Research, Oxford Instruments) was used to image the topography of the as-grown samples. All samples were scanned in AC mode (tapping mode) in ambient conditions. AFM probes of RTESPA-150 and PFQNE-AL were typically used for the scanning.

Scanning near-field optical microscopy (SNOM). A home-built SNOM setup (main components include: Innova AFM, Bruker; L3S CO_2 laser, Access Laser and KLD-0.1-J1 MCT detector, Kolmar) was used to detect the infrared response of the as-grown samples. Infrared beam of 10.6 μm was focused onto the apex of a gold-coated AFM tip (MikroMasch HQ:NSC35/Cr-Au). The near-field at the apex was strongly enhanced by the tapped tip, leading to a strong local interaction of light with material that underneath the tip. The scattered light with local optical information of the sample was collected by an infrared detector. Near-field optical images with spatial resolution better than 20 nm can be achieved with sharp AFM tips.

Calculations of free energy of formation and growth phase diagram. In this work, we mainly concentrated on the role of the presence of h-BN substrate and H_2 partial pressure during the growth, which determines either GNR or CNT is the thermodynamically favorable species to be nucleated. To include the influence of h-BN substrate and H_2 partial pressure on the selective nucleation of GNR or CNT, we first considered their difference in the van der Waals adhesions with h-BN substrate, as shown in Fig. 3a where a GNR has a large contact area with the substrate but only the bottom part of a CNT is in contact with the substrate. For CNT, there is extra curvature energy; while for GNR, there is extra hydrogen termination (Fig. 3a). Evaluating all the three energy terms, we obtained the phase diagram that shows, under the growth conditions (temperature and H_2 pressure), which one (GNR or CNT) is energetically more favorable, and is more likely to be synthesized.

All DFT calculations were performed using the Vienna Ab initio Simulation Package (VASP)[38–40] with projected augmented wave (PAW) method[41]. The generalized gradient exchange–correlation functional approximation (GGA)[42] was employed with the D3 dispersion correction[43] in order to precisely describe van der Waals interactions. The plane-wave cutoff energy was set to be 600 eV and the Brillouin zone was sampled using Monkhorst–Pack k-mesh with a separation criterion of 0.02[44]. Criteria for energy and force convergence were set to be 10^{-4} eV and 10^{-2} eV/Å, respectively.

To compare the thermodynamic stability of GNRs and CNTs at growth condition, we included the influence of temperature and pressure to the system, and estimated the free energy of GNR formation by the following equation[45,46]:

$$\Delta G_f(\mathrm{GNR}) = E_f(\mathrm{GNR}) + \Delta F_{vib} - \frac{1}{2} N_H \times \mu_{H_2}, \tag{1}$$

where $E_f(\mathrm{GNR})$, ΔF_{vib} N_H and μ_{H_2} are the ground state (0 K) formation energy of GNRs, vibrational contribution of the hydrogen termination at GNR edge, number of hydrogen atoms at edge, and hydrogen chemical potential in gas phase. The vibrational contribution term was estimated with the following equation[47]:

$$\Delta F_{\mathrm{vib}} = \sum\nolimits_{\omega} h\omega \left(\frac{1}{2} + \frac{1}{e^{\beta h\omega} - 1} \right) - k_B T \left[\frac{\beta h\omega}{e^{\beta h\omega} - 1} - \ln(1 - e^{-\beta h\omega}) \right], \tag{2}$$

where ω and h are the phonon frequency and Plank's constant, and $\beta = (k_B T)^{-1}$. The third term on the right of Eq. (1) was estimated by bellow equation[46]:

$$\mu_{H_2} = H^0(T) - H^0(0\ \mathrm{K}) - TS^0(T) + k_B T \ln \frac{P_{H_2}}{P_0}, \tag{3}$$

where, the standard values, $H^0(T)$, $H^0(0\ \mathrm{K})$, and $S^0(T)$ are obtained from chemical tables[48], P_0 is atmospheric pressure, and P_{H_2} is experimental hydrogen pressure.

Data availability

The datasets used during the current study available from the corresponding author on reasonable request.

Received: 20 December 2022; Accepted: 14 March 2023
Published online: 15 March 2023

References

1. Castro Neto, A. H., Guinea, F., Peres, N. M. R., Novoselov, K. S. & Geim, A. K. The electronic properties of graphene. *Rev. Mod. Phys.* **81**, 109–162. https://doi.org/10.1103/RevModPhys.81.109 (2009).
2. Laird, E. A. *et al.* Quantum transport in carbon nanotubes. *Rev. Mod. Phys.* **87**, 703–764. https://doi.org/10.1103/RevModPhys.87.703 (2015).
3. Son, Y.-W., Cohen, M. L. & Louie, S. G. Energy gaps in graphene nanoribbons. *Phys. Rev. Lett.* **97**, 216803. https://doi.org/10.1103/PhysRevLett.97.216803 (2006).
4. Lee, C., Wei, X. D., Kysar, J. W. & Hone, J. Measurement of the elastic properties and intrinsic strength of monolayer graphene. *Science* **321**, 385–388. https://doi.org/10.1126/science.1157996 (2008).
5. Yu, M. F. *et al.* Strength and breaking mechanism of multiwalled carbon nanotubes under tensile load. *Science* **287**, 637–640. https://doi.org/10.1126/science.287.5453.637 (2000).
6. Balandin, A. A. *et al.* Superior thermal conductivity of single-layer graphene. *Nano Lett.* **8**, 902–907. https://doi.org/10.1021/nl073 1872 (2008).
7. Javey, A., Guo, J., Wang, Q., Lundstrom, M. & Dai, H. J. Ballistic carbon nanotube field-effect transistors. *Nature* **424**, 654–657. https://doi.org/10.1038/nature01797 (2003).
8. Baringhaus, J. *et al.* Exceptional ballistic transport in epitaxial graphene nanoribbons. *Nature* **506**, 349–354. https://doi.org/10.1038/nature12952 (2014).
9. Tans, S. J., Verschueren, A. R. M. & Dekker, C. Room-temperature transistor based on a single carbon nanotube. *Nature* **393**, 49–52 (1998).
10. Yang, L., Park, C. H., Son, Y. W., Cohen, M. L. & Louie, S. G. Quasiparticle energies and band gaps in graphene nanoribbons. *Phys. Rev. Lett.* **99**, 186801. https://doi.org/10.1103/PhysRevLett.99.186801 (2007).
11. Fujita, M., Wakabayashi, K., Nakada, K. & Kusakabe, K. Peculiar localized state at zigzag graphite edge. *J. Phys. Soc. Jpn.* **65**, 1920–1923. https://doi.org/10.1143/jpsj.65.1920 (1996).
12. Nakada, K., Fujita, M., Dresselhaus, G. & Dresselhaus, M. S. Edge state in graphene ribbons: Nanometer size effect and edge shape dependence. *Phys. Rev. B Condens. Matter* **54**, 17954–17961. https://doi.org/10.1103/PhysRevB.54.17954 (1996).
13. Blackwell, R. E. *et al.* Spin splitting of dopant edge state in magnetic zigzag graphene nanoribbons. *Nature* **600**, 647. https://doi.org/10.1038/s41586-021-04201-y (2021).
14. Magda, G. Z. *et al.* Room-temperature magnetic order on zigzag edges of narrow graphene nanoribbons. *Nature* **514**, 608. https://doi.org/10.1038/nature13831 (2014).
15. Iijima, S. Helical microtubules of graphitic carbon. *Nature* **354**, 56–58. https://doi.org/10.1038/354056a0 (1991).
16. Bethune, D. S. *et al.* Cobalt-catalysed growth of carbon nanotubes with single-atomic-layer walls. *Nature* **363**, 605–607. https://doi.org/10.1038/363605a0 (1993).
17. Guo, T., Nikolaev, P., Thess, A., Colbert, D. T. & Smalley, R. E. Catalytic growth of single-walled nanotubes by laser vaporization. *Chem. Phys. Lett. (Netherlands)* **243**, 49–54. https://doi.org/10.1016/0009-2614(95)00825-o (1995).
18. Ebbesen, T. W. & Ajayan, P. M. Large-scale synthesis of carbon nanotubes. *Nature* **358**, 220–222. https://doi.org/10.1038/358220a0 (1992).
19. Zheng, L. X. *et al.* Ultralong single-wall carbon nanotubes. *Nat. Mater.* **3**, 673–676. https://doi.org/10.1038/nmat1216 (2004).
20. Jin, Z. *et al.* Ultralow feeding gas flow guiding growth of large-scale horizontally aligned single-walled carbon nanotube arrays. *Nano Lett.* **7**, 2073–2079. https://doi.org/10.1021/nl070980m (2007).
21. Zhang, R. *et al.* Growth of half-meter long carbon nanotubes based on Schulz–Flory distribution. *ACS Nano* **7**, 6156–6161. https://doi.org/10.1021/nn401995z (2013).
22. Gao, Q. *et al.* Detection of chirality of single-walled carbon nanotubes on hexagonal boron nitride. *Appl. Phys. Lett.* **117**, 023101. https://doi.org/10.1063/5.0005831 (2020).
23. Cai, J. *et al.* Atomically precise bottom-up fabrication of graphene nanoribbons. *Nature* **466**, 470–473. https://doi.org/10.1038/nature09211 (2010).
24. Han, M. Y., Oezyilmaz, B., Zhang, Y. & Kim, P. Energy band-gap engineering of graphene nanoribbons. *Phys. Rev. Lett.* **98**, 206805. https://doi.org/10.1103/PhysRevLett.98.206805 (2007).
25. Li, X., Wang, X., Zhang, L., Lee, S. & Dai, H. Chemically derived, ultrasmooth graphene nanoribbon semiconductors. *Science* **319**, 1229–1232. https://doi.org/10.1126/science.1150878 (2008).
26. Kosynkin, D. V. *et al.* Longitudinal unzipping of carbon nanotubes to form graphene nanoribbons. *Nature* **458**, 872–875. https://doi.org/10.1038/nature07872 (2009).
27. Wang, X. & Dai, H. Etching and narrowing of graphene from the edges. *Nat. Chem.* **2**, 661–665. https://doi.org/10.1038/nchem.719 (2010).
28. Sprinkle, M. *et al.* Scalable templated growth of graphene nanoribbons on SiC. *Nat. Nanotechnol.* **5**, 727–731. https://doi.org/10.1038/nnano.2010.192 (2010).
29. Jacobberger, R. M. *et al.* Direct oriented growth of armchair graphene nanoribbons on germanium. *Nat. Commun.* **6**, 8006. https://doi.org/10.1038/ncomms9006 (2015).
30. Wang, H. S. *et al.* Towards chirality control of graphene nanoribbons embedded in hexagonal boron nitride. *Nat. Mater.* **20**, 202. https://doi.org/10.1038/s41563-020-00806-2 (2021).
31. Lyu, B. S. *et al.* Catalytic growth of ultralong graphene nanoribbons on insulating substrates. *Adv. Mater.* **34**, 2200956. https://doi.org/10.1002/adma.202200956 (2022).
32. Shi, Z. *et al.* Observation of a Luttinger-liquid plasmon in metallic single-walled carbon nanotubes. *Nat. Photonics* **9**, 515–519. https://doi.org/10.1038/nphoton.2015.123 (2015).
33. Gavillet, J. *et al.* Root-growth mechanism for single-wall carbon nanotubes. *Phys. Rev. Lett.* **87**, 275504. https://doi.org/10.1103/PhysRevLett.87.275504 (2001).
34. Ding, L. P. *et al.* Why carbon nanotubes grow. *J. Am. Chem. Soc.* **144**, 5606–5613. https://doi.org/10.1021/jacs.2c00879 (2022).
35. Liu, Y., Dobrinsky, A. & Yakobson, B. I. Graphene edge from armchair to zigzag: The origins of nanotube chirality?. *Phys. Rev. Lett.* **105**, 235502. https://doi.org/10.1103/PhysRevLett.105.235502 (2010).
36. Wei, D. *et al.* Controllable unzipping for intramolecular junctions of graphene nanoribbons and single-walled carbon nanotubes. *Nat. Commun.* **4**, 1374. https://doi.org/10.1038/ncomms2366 (2013).
37. Xu, Z., Qiu, L. & Ding, F. The kinetics of chirality assignment in catalytic single-walled carbon nanotube growth and the routes towards selective growth. *Chem. Sci.* **9**, 3056–3061. https://doi.org/10.1039/c7sc04714b (2018).

38. Kresse, G. & Hafner, J. Ab initio molecular dynamics for open-shell transition metals. *Phys. Rev. B* **48**, 13115–13118. https://doi.org/10.1103/PhysRevB.48.13115 (1993).
39. Kresse, G. & Furthmüller, J. Efficiency of ab-initio total energy calculations for metals and semiconductors using a plane-wave basis set. *Comput. Mater. Sci.* **6**, 15–50. https://doi.org/10.1016/0927-0256(96)00008-0 (1996).
40. Wu, P. *et al.* Carbon dimers as the dominant feeding species in epitaxial growth and morphological phase transition of graphene on different Cu substrates. *Phys. Rev. Lett.* **114**, 216102. https://doi.org/10.1103/PhysRevLett.114.216102 (2015).
41. Kresse, G. & Joubert, D. From ultrasoft pseudopotentials to the projector augmented-wave method. *Phys. Rev. B* **59**, 1758–1775. https://doi.org/10.1103/PhysRevB.59.1758 (1999).
42. Perdew, J. P., Burke, K. & Ernzerhof, M. Generalized gradient approximation made simple. *Phys. Rev. Lett.* **77**, 3865–3868. https://doi.org/10.1103/PhysRevLett.77.3865 (1996).
43. Grimme, S., Antony, J., Ehrlich, S. & Krieg, H. A consistent and accurate ab initio parametrization of density functional dispersion correction (DFT-D) for the 94 elements H-Pu. *J. Chem. Phys.* **132**, 154104. https://doi.org/10.1063/1.3382344 (2010).
44. Monkhorst, H. J. & Pack, J. D. Special points for Brillouin-zone integrations. *Phys. Rev. B* **13**, 5188–5192. https://doi.org/10.1103/PhysRevB.13.5188 (1976).
45. Shu, H., Chen, X. & Ding, F. The edge termination controlled kinetics in graphene chemical vapor deposition growth. *Chem. Sci.* **5**, 4639–4645. https://doi.org/10.1039/C4SC02223H (2014).
46. Gao, J. & Ding, F. First-principles phase diagram of magic-sized carbon clusters on Ru(0001) and Rh(111) surfaces. *J. Phys. Chem. C* **119**, 11086–11093. https://doi.org/10.1021/jp5118536 (2015).
47. Reuter, K. & Scheffler, M. Composition, structure, and stability of RuO2(110) as a function of oxygen pressure. *Phys. Rev. B* **65**, 035406. https://doi.org/10.1103/PhysRevB.65.035406 (2002).
48. Chase, M. *NIST-JANAF Thermochemical Tables* 4th edn. (American Institute of Physics, 1998).

Acknowledgements

This work is supported by the National Key R&D Program of China (No. 2021YFA1202902), the National Natural Science Foundation of China (No. 12074244), the open research fund of Songshan Lake Materials Laboratory (No.2021SLABFK07), by the Institute for Basic Science (IBS-R019-D1) of South Korea and by "Shuguang Program" supported by Shanghai Education Development Foundation and Shanghai Municipal Education Commission. K.W. and T.T. acknowledge support from the Elemental Strategy Initiative conducted by the MEXT, Japan, Grant Number JPMXP0112101001, JSPS KAKENHI (Grant Numbers 19H05790, 20H00354) and A3 Foresight by JSPS. Z.S. acknowledges support from SJTU (21X010200846), and additional support from a Shanghai talent program. B.L. acknowledges support from the Development Scholarship for Outstanding Ph.D. of Shanghai Jiao Tong University.

Author contributions

S.L., B.L., J.C., F.D. and Z.S. conceived the project. Z.S. and F.D. supervised the project. S.L., B.L. and J.C. grew the samples and carried out AFM measurements. L.Q. and F.D. calculated the growth phase diagram. K.W. and T.T. grew h-BN single crystals. S.L., B.L., J.C., L.Q., S.M., P.S., Z.Z., Y.X., Q.L., F.D. and Z.S. analyzed the data. S.L. and Z.S. wrote the paper with input from all authors. All authors discussed the results and commented on the manuscript.

Competing interests

The authors declare no competing interests.

Additional information

Supplementary Information The online version contains supplementary material available at https://doi.org/10.1038/s41598-023-31573-0.

Correspondence and requests for materials should be addressed to F.D. or Z.S.